Microfluidic Crystal Engineering of π-Conjugated Polymers
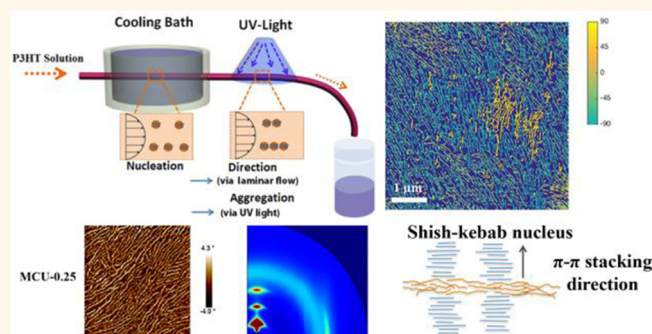
Gang Wang,[†,||] Nils Persson,[†] Ping-Hsun Chu,[†] Nabil Kleinhenz,[‡] Boyi Fu,[†] Mincheol Chang,[†] Nabankur Deb,[§] Yimin Mao,[⊥] Hongzhi Wang,*[,||] Martha A. Grover,*[,†] and Elsa Reichmanis*[,†,‡,§]

[†]School of Chemical and Biomolecular Engineering, [‡]School of Chemistry and Biochemistry, and [§]School of Materials Science and Engineering, Georgia Institute of Technology, Atlanta, Georgia 30332, United States, [||]State Key Laboratory for Modification of Chemical Fibers and Polymer Materials, College of Material Science and Engineering, Donghua University, Shanghai 201620, People's Republic of China, and [⊥]NIST Center for Neutron Research, National Institute of Standards and Technology, Gaithersburg, Maryland 20899, United States

ABSTRACT Very few studies have reported oriented crystallization of conjugated polymers directly in solution. Here, solution crystallization of conjugated polymers in a microfluidic system is found to produce tightly π-stacked fibers with commensurate improved charge transport characteristics. For poly(3-hexylthiophene) (P3HT) films, processing under flow caused exciton bandwidth to decrease from 140 to 25 meV, $\pi-\pi$ stacking distance to decrease from 3.93 to 3.72 Å and hole mobility to increase from an average of 0.013 to 0.16 cm^2 V^{-1} s^{-1}, vs films spin-coated from pristine, untreated solutions. Variation of the flow rate affected thin-film structure and properties, with an intermediate flow rate of 0.25 m s^{-1} yielding the optimal $\pi-\pi$ stacking distance and mobility. The flow process included sequential cooling followed by low-dose ultraviolet irradiation that promoted growth of conjugated polymer fibers. Image analysis coupled with mechanistic interpretation supports the supposition that "tie chains" provide for charge transport pathways between nanoaggregated structures. The "microfluidic flow enhanced semiconducting polymer crystal engineering" was also successfully applied to a representative electron transport polymer and a nonhalogenated solvent. The process can be applied as a general strategy and is expected to facilitate the fabrication of high-performance electrically active polymer devices.

KEYWORDS: microfluidic · crystal engineering · conjugated polymer · charge transport mobility · tie-chains

The solution processability of conjugated polymer semiconductors has enabled the development of organic electronic devices, including organic photovoltaics (OPV), light-emitting diodes (OLED), and organic field-effect transistors (OFET), which can be fabricated over large areas at low cost.[1−5] However, enhancement of organic semiconductors' charge transport properties is crucial to their use in these applications. While there are ongoing efforts to synthesize novel high-mobility conjugated polymers, precise manipulation of crystallization, aggregation and orientation of the material during processing is essential for both optimized and reproducible device performance.[2,6−9] To this end, poly-(3-hexylthiophene) (P3HT) is widely used as a model material to study the effect of process variables on both device performance and the aggregation mechanisms that give rise to microstructural order.

Over the past decade, doctor blading, dip coating,[10] strain stretching,[11] poor solvent addition,[12] topographical patterning,[13] and thermal[14] or solvent vapor[15] annealing, among many others, have all been shown to cause significant enhancement of the charge carrier mobility in π-conjugated polymer-based OFET devices.

Although many of these processing techniques are infeasible on an industrial scale, the results of these studies have revealed the microstructural features that give rise to high-mobility devices: (i) highly ordered crystals with a high degree of electronic delocalization,[16] (ii) edge-on orientation relative to the dielectric surface,[17,18] and (iii) long-range interconnectivity between crystalline domains to form a percolation network for charge transport on the device scale.[19,20] Microfluidic technology has been widely applied to the controlled nucleation and crystallization of small molecule

conjugated materials, proteins and drug molecules (e.g., aspirin and acetaminophen).[21−23] Very few studies have reported oriented crystallization of conjugated polymers directly in solution.

Here, a general fluid processing strategy to induce oriented conjugated polymer aggregation is demonstrated, with a correspondingly large increase in polymer charge transport characteristics. This scalable approach allows for precise control of conjugated polymer self-assembly in a preprocessing system that could, without significant additional effort, be linked directly to thin film deposition as a continuous flow process. Image analysis coupled with mechanistic interpretation supports the supposition that "tie chains" provide for charge transport pathways between nanoaggregated structures. The results also point to a platform that could be used to further elucidate the complex mechanisms underlying the self-assembly of conjugated polymers that give rise to their structure and properties. Microstructural analysis of semiconducting polymer thin-films indicated that enhanced intermolecular aggregation, better orientation (both nanoscale and long-range), and narrower $\pi-\pi$ stacking distance were achieved. The enhanced crystallization that results from distinctive shear forces produced by a laminar flow field provide insight into the conjugated polymer crystallization and the mechanism of formation of polycrystalline structures that are favorable to charge transport.[24]

The approach is generic and can be applied to different solvent/conjugated-polymer systems. Various solvents, halogenated (chloroform, $CHCl_3$) and non-halogenated (toluene), and polymers, hole-transport (P3HT) and electron-transport (naphthaplene diimide based conjugated polymer, poly(NDI2OD-T2)), were tested, and enhanced mobility was achieved. Microfluidic processing offers (i) rapid mass and heat transfer, (ii) accurate control of process residence times in a flow system, (iii) no solvent evaporation in the confined microchannels, and (iv) parallel scalability,[25−29] providing a facile and general high-throughput processing strategy for polymer-based devices for a range of applications.

RESULTS

P3HT OFET Device Performance. Figure 1a depicts the experimental microfluidic-cooling-UV (MCU) processing sequence, which was first evaluated using P3HT/$CHCl_3$ (5 mg mL^{-1}). The solution was passed through the microfluidic channel comprising two sections: flow-cooling (residence time 1 s, 0 °C) followed by flow-UV (15 s, 23 °C). Three different flow rates were tested: MCU-0.10 (0.10 m s^{-1}), MCU-0.25 (0.25 m s^{-1}), and MCU-0.60 (0.60 m s^{-1}). The residence time can be fixed by tuning the length of microchannel for different flow rates. The resulting solutions were stored in a sealed vial prior to transistor fabrication. Bottom gate, bottom contact OFETs (Figure 1b) were fabricated by

spin-coating the respective P3HT solutions onto device substrates (transistor length = 50 um and channel width = 2000 um). A control experiment with no flow termed cooling-UV (CU) was performed in which a static polymer solution was cooled in a bath at 0 °C for 30 s, then irradiated using a UV lamp for 6 min. The gel permeation chromatography (GPC) (Table S1) and ^{1}H nuclear magnetic resonance (^{1}H NMR) (Figure S2) analysis were used to confirm that the process does not induce chemical/molecular structural changes.

Figure 1c and d depicts transfer and output curves, which are typical of p-channel OFET operation in the accumulation mode; and Figure 1e presents the calculated mobilities. Both the presence of flow and the flow rate had a significant effect on the mobility. At the optimal flow rate of 0.25 m s^{-1}, the average mobility reached as high as 0.16 cm^2 V^{-1} s^{-1}, with a maximum of 0.18 cm^2 V^{-1} s^{-1}. While static CU processing afforded approximately a 5-fold increase in mobility (from $1.3 \pm 0.15 \times 10^{-2}$ to $6.58 \pm 1.05 \times 10^{-2}$ cm^2 V^{-1} s^{-1}), MCU processing provided for more than a 13-fold performance enhancement (from $1.3 \pm 0.15 \times 10^{-2}$ to $16 \pm 1.85 \times 10^{-2}$ cm^2 V^{-1} s^{-1}). Table 1 presents the average mobilities obtained for P3HT processed using the microfluidic approach vs those from control experiments, which confirm the advantages associated with the combination of cooling and UV irradiation under fluid flow conditions.

UV−Visible Characterization. Figure 2a and b depicts the electronic absorption spectra obtained from P3HT/$CHCl_3$ solutions via different processing protocols and the corresponding semiconducting thin-films, respectively. The solutions changed from bright orange to dark brown upon both CU and MCU processing (conditions 7−9 in Table 1), indicative of an increase in the extent of P3HT nanoaggregation.[30] In addition, the solution aggregates after MCU processing are thermally reversible (see Figure S3). The solution-based absorption spectra exhibit low energy features at ca. 570 and 620 nm, characteristic of vibronic bands associated with the (0−1) and (0−0) transitions, respectively. The emergence of these features is believed to be associated with an increase in ordered aggregates formed via $\pi-\pi$ stacking between polymer chains in solution (see Figure 3a, *vide infra*).[30,31]

As discerned from Figure 2b, MCU processing appears to effect an increase in intensity of the low energy (0−1) and (0−0) absorption bands in resultant polymer films. Thus, consistent with previous reports,[30,32] nanoaggregates formed in the solution appear to survive the spin-coating process, and in turn provide for increased molecular order in the solid thin-films. In addition, MCU processing effects a red-shift in P3HT absorption peaks compared to those from pristine and CU processed films, which suggests enhanced cofacial $\pi-\pi$ stacking and/or planarization of the conjugated backbone.[30−32] According to Spano's model,[31] interchain
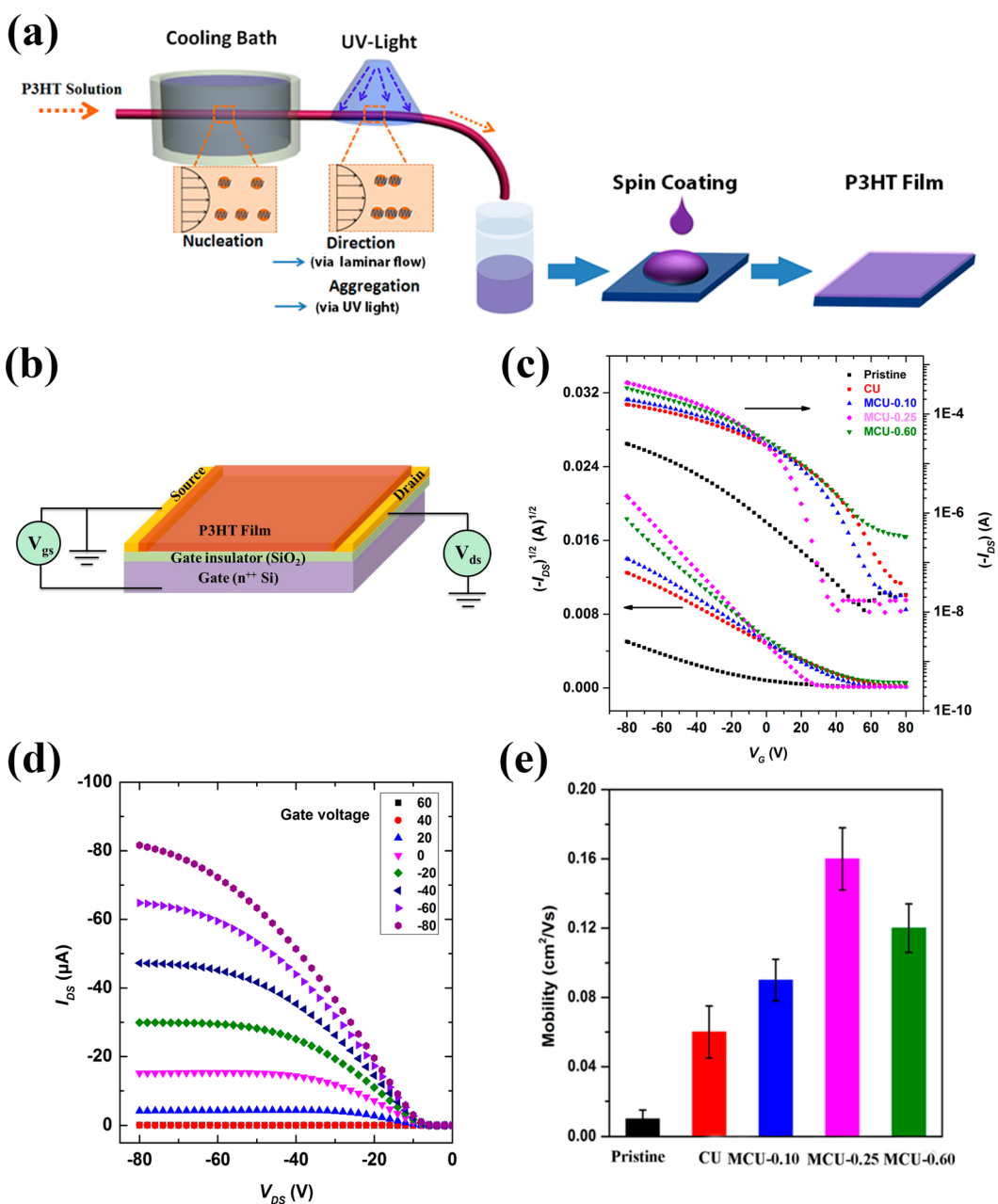
Figure 1. (a) Experimental diagram of the MCU-process sequence. (b) Schematic representation of OFET device architecture. (c) Transfer characteristics of P3HT OFETs fabricated from polymer solutions using different processing methods. (d) Typical output characteristics obtained from a P3HT OFET prepared via spin-coating from P3HT/CHCl₃ solution via MCU-0.25 processing. (e) Average field-effect mobilities of P3HT films spin-coated from P3HT/CHCl₃ solutions via different processing methods. Mobilities were calculated in the saturation regime of operation with $V_{DS}= -80$ V. Five sets of devices were fabricated for each set of conditions; five devices were characterized in each run.

coupling leads to vibronic bands in the absorption spectrum. Further, the vibronic bands can be related to the free exciton bandwidth (W), which correlates with intrachain ordering of an individual polymer chain within the aggregates.[33,34] An increase in intramolecular order is associated with a decrease in W, and is used as a general method to compare the extent of conjugation in polymer based semiconductors. Equation 1 is used to calculate the W values, using the intensities of the (0−0) and (0−1) transitions obtained from fits to the experimental spectra (see Figures S4 in the

Supporting Information).

$$\frac{I_{0-0}}{I_{0-1}} = \left\{ \frac{1 - 0.24W/E_{p}}{1 + 0.073W/E_{p}} \right\}^{2} \quad (1)$$

I_{0-0} and I_{0-1} represent the intensities of the (0−0) and (0−1) transitions, respectively, and E_{p} is the vibrational energy of the symmetric vinyl stretch (taken as 0.18 eV). As shown in Figure 2c, the value of W for P3HT films obtained from pristine solutions appears at 140 meV, but significantly decreases to 110, 65, 25, and 67 meV after CU, MCU-0.10, MCU-0.25, and MCU-0.60,

TABLE 1. Average Mobility Obtained for the Range of Solution Process Conditions, Including Pristine, Cooling, UV, Extended Cooling-UV, Flow-Cooling, Flow-UV, and MCU Processing[a]

	cooling (time)	UV (time)	flow rate (m s^{-1})	average mobility (cm^2 V^{-1} s^{-1})	standard deviation (cm^2 V^{-1} s^{-1})
1 (pristine)	no	no	0	0.013	0.15 × 10^{-2}
2 (static cooling)	30 s	no	0	0.025	0.52 × 10^{-2}
3 (static UV)	no	6 min	0	0.05	0.89 × 10^{-2}
4 (static cooling-UV)	30 s	6 min	0	0.065	1.05 × 10^{-2}
5 (flow-cooling)	1 s	no	0.25	0.02	0.21 × 10^{-2}
6 (flow-UV)	no	15 s	0.25	0.11	1.22 × 10^{-2}
7 (MCU-0.10)	1 s	15 s	0.10	0.09	1.14 × 10^{-2}
8 (MCU-0.25)	1 s	15 s	0.25	0.16	1.85 × 10^{-2}
9 (MCU-0.60)	1 s	15 s	0.60	0.12	1.32 × 10^{-2}

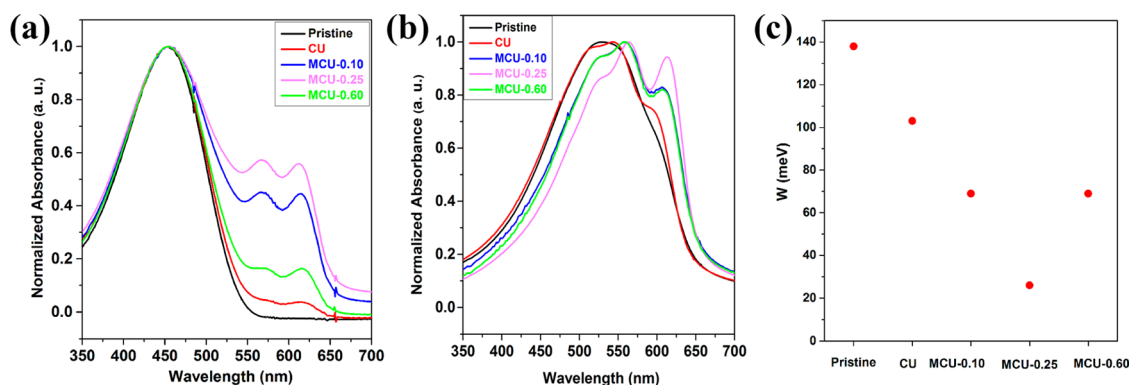[a] Five devices were characterized in each run.

Figure 2. Normalized UV−visible absorption spectra of (a) P3HT/CHCl$_3$ solutions and (b) corresponding P3HT films obtained by spin-coating. (c) Evolution of exciton bandwidth W of ordered aggregates in the films as a function of various processing methods.

respectively, indicative of enhanced intramolecular thin-film P3HT ordering. In addition, the intensity of the low energy features varies with flow rate (Figure 2a and b). The lowest free exciton bandwidth can be observed at a flow rate of 0.25 m s^{-1} for solidified thin-films, suggesting that these conditions provide for the most well-ordered polymer aggregates.

Microstructural Characterization. Atomic force microscopy (AFM) phase images of P3HT films obtained from pristine, CU, and MCU processed P3HT solutions are shown in Figure 3a−e, demonstrating the microstructural evolution from a pristine, featureless film to a heterogeneous, anisotropic film with clearly defined P3HT nanofibers. For static cooling-UV processing, nanofibrillar structures, ca. 20 nm in width and 500−800 nm in length, can be observed. Microfluidic processing effected an increase in fiber size and density, with concomitant alignment. The microstructure was also influenced by flow rate. At the flow rate of 0.10, 0.25, and 0.60 m s^{-1}, the nanofibers are 600−1200 nm, 1.2−1.8 μm, and 500−800 nm in length, respectively. The AFM images convey the importance of fluid flow and flow rate in the development of thin-film morphology.

Grazing-incidence wide-angle X-ray scattering (GIWAXS) was used to further investigate the improved structural orientation and $\pi-\pi$ stacking of MCU processed P3HT films.[18,35] GIWAXS images showed as collected diffraction pattern on detector (see Figure S1 for 2-D correction of images). Common to all GIWAXS patterns shown in Figure 3f−j is that three (h00) reflection arcs ((100), (200), (300)) appear in the out-of-plane (q_z) direction, indicating that the a-axis (P3HT lamellar plane packing direction) is perpendicular to the substrate.[18,36,37] Similarly, peaks along the b-axis correspond to the $\pi-\pi$ stacking direction, hence the peak corresponding to the (010) plane provides direct information about the $\pi-\pi$ stacking distance. The degree of orientation of the crystal planes and domain size may vary, depending on breadth of intensity distribution of the peak along the polar angle (Φ) (Herman's orientation factor), and on the width of the line profile along q_z (Scherrer's equation), respectively. The position of the GIWAXS peaks suggests the orientation of the P3HT crystal planes in these samples is primarily edge-on, which places the highest mobility charge transport pathways in the region of the semi-conducting film where transport occurs.[36,38]

As seen in Figure 3f, the pristine sample already shows well-defined orientation as described. The (010) peak, however, is not visible, which suggests either small crystal size and/or significant effects associated with disorder among $\pi-\pi$ stacks. With flow, the (010)
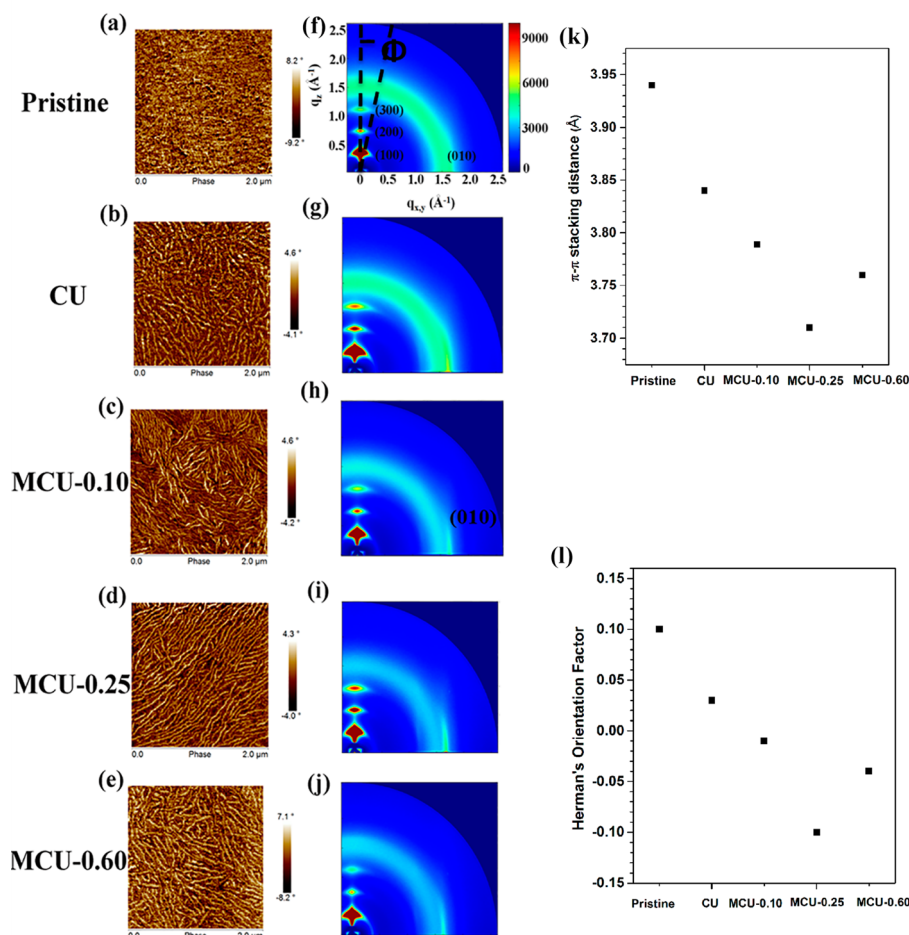
Figure 3. (a−e) Tapping mode AFM phase images ($2 \times 2 \ \mu m^2$). (f−j) Synchrotron GIWAXS from P3HT films on silicon wafers with no processing, CU, MCU-0.10, MCU-0.25, MCU-0.60, and respectively. (k) $\pi-\pi$ stacking distance and (l) Herman's orientation factor of P3HT films with different processing methods.
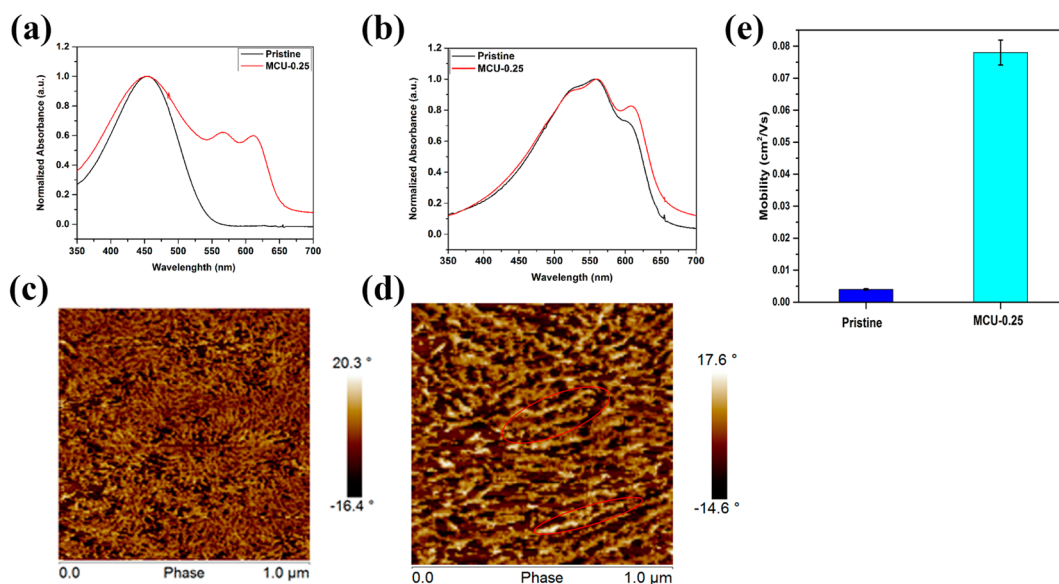
plane gradually becomes more pronounced. The MCU-0.25 flow rate was found to optimize both $\pi-\pi$ stacking distance and edge-on orientation, as evidenced by the calculated crystal spacings and orientation factors (Figure 3k, l). The (010) peak position changes from 0.25 $Å^{-1}$ for pristine films to 0.27 $Å^{-1}$ for MCU-0.25 processed P3HT, corresponding to a reduction of the $\pi-\pi$ stacking distance from 3.93 to 3.72 Å (Figure 3i). In addition, the Herman's orientation parameter for the (010) plane shifts to a more negative value when MCU processing was applied, which suggests enhanced edge-on orientation (Figure 3l). At a flow rate of 0.25 m s^{-1}, the Herman's orientation factor drops to −0.10 vs values of −0.01 and −0.04 for flow rates of 0.01 and 0.60 m s^{-1}, respectively. These results again point to the flow rate of 0.25 m s^{-1} as being optimum.

It is known that thiophene ring orientation and $\pi-\pi$ stacking distance significantly impact charge carrier mobility.[37,39] Analysis of GIWAXS and AFM data demonstrated that MCU processing can enhance fiber growth, shorten P3HT $\pi-\pi$ stacking distance, and enhance edge-on orientation. All of these microstructural features are expected to confer the films with more efficient charge carrier transport pathways, providing the potential for improved macroscopic semiconductor device performance.

The MCU process is not restricted to use with P3HT/CHCl$_3$. The method appears equally applicable to nonchlorinated solvents and alternate conjugated polymers. Specifically, conjugated polymer charge carrier mobility of MCU processed P3HT/toluene solutions is also significantly increased with respect to that of similar solutions processed by standard methods (Figure 4). P3HT/toluene absorption spectra exhibit low energy features at about 570 and 620 nm, characteristic of well-ordered aggregate formation (Figure 4a); and the solution based nanoaggregates survive a spin-coating process (Figure 4b). MCU processed solidified films exhibit enhanced crystallinity (Figure 4c), AFM imaging reveals that the films are comprised of noticeably wider and longer fibrils than the pristine counterparts (Figure 4d), and fibrillar aggregates (indicated with red oval) are present (Figure 4d). As shown in Figure 4e, mobility increased by a factor of 15, from $0.40 \pm 0.022 \times 10^{-2}$ to $7.5 \pm 0.42 \times 10^{-2}$ cm^2 V^{-1} s^{-1}.

P3HT in toluene

(a)

(b)

(e)

(c)

(d)

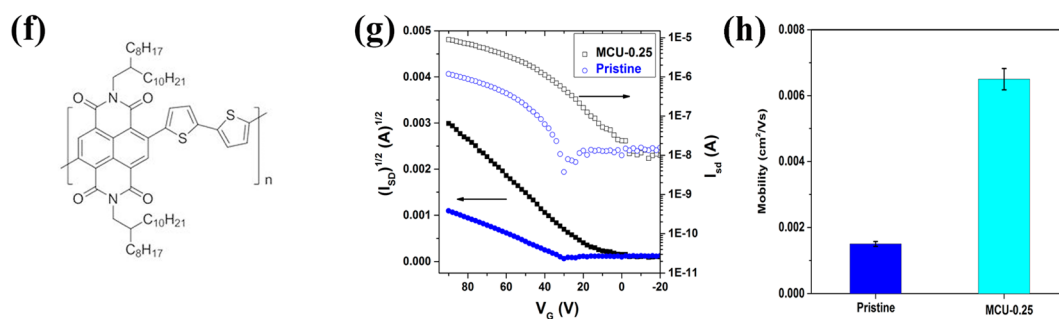## Electron-transport polymer

(f)

(g)

(h)

Figure 4. Normalized UV−visible absorption spectra of (a) P3HT/toluene solutions before and after MCU processing at the flow rate of 0.25 m s^{-1}. (b) Corresponding P3HT films obtained by spin-coating. Tapping mode AFM phase images ($1 \times 1\ \mu m^2$) of P3HT films obtained by spin-coating from P3HT/toluene solutions (c) before and (d) after MCU processing at a flow rate of 0.25 m s^{-1}. (e) Field-effect mobilities of corresponding films. (f) Chemical structure of naphthaplene diimide based conjugated polymer poly(NDI2OD-T2). (g) Transfer characteristics of poly(NDI2OD-T2) OFETs fabricated from polymer solutions with different processing methods. (h) Average field-effect mobilities of poly(NDI2OD-T2) films spin-coated from poly(NDI2OD-T2) solutions via different processing methods. Mobilities were calculated in the saturation regime of operation with $V_{DS} = 90$ V.

Electron transporting conjugated polymers are also crucial to the development of functional organic electronic devices, and to this end, novel polymers have been demonstrated recently in the literature.[40] Poly(NDI2OD-T2), a typical electron transport conjugated polymer, was utilized to test the applicability of MCU processing to alternate polymer systems. As shown in Figure 4h, MCU-0.25, effected a 5-fold increase in mobility ($1.3 \pm 0.2 \times 10^{-3}$ vs $6.2 \pm 0.42 \times 10^{-3}$ cm^2 V^{-1} s^{-1}). Further enhancements are expected with process optimization.

DISCUSSION

The Flow Environment. A Reynolds number (*Re*) of less than 2000 indicates a laminar flow regime. Even at the highest fluid flow rate of 0.60 m s^{-1}, *Re* is ca. 42, indicating a laminar flow environment for all flow experiments. Although polymer solutions display complex non-Newtonian properties, they will still experience a shear field with radial dependence in tubular flow, with maximum velocity at the center of the tube.[41] An increase in fluid flow rate causes an increase in the shear force experienced by the solution. Figure 5a shows the microfluidic channel as viewed through crossed polarizers during solution flow as the channel is rotated from 0° to 45° with respect to the analyzer. While an isotropic material would appear dark at all angles, the observed transmitted light intensity indicates a birefringent fluid with requisite anisotropy.[42] The near complete extinction and reemergence of brightness upon rotation of the channel long axis from 0° to 45° suggests long-range ordering over the dimensions of the microchannel. Figure 5b depicts the linear dichroism displayed by P3HT solutions in a glass capillary at the end of the microfluidic channel, after UV radiation, while still under flow. Dichroism was not evident for pristine solutions
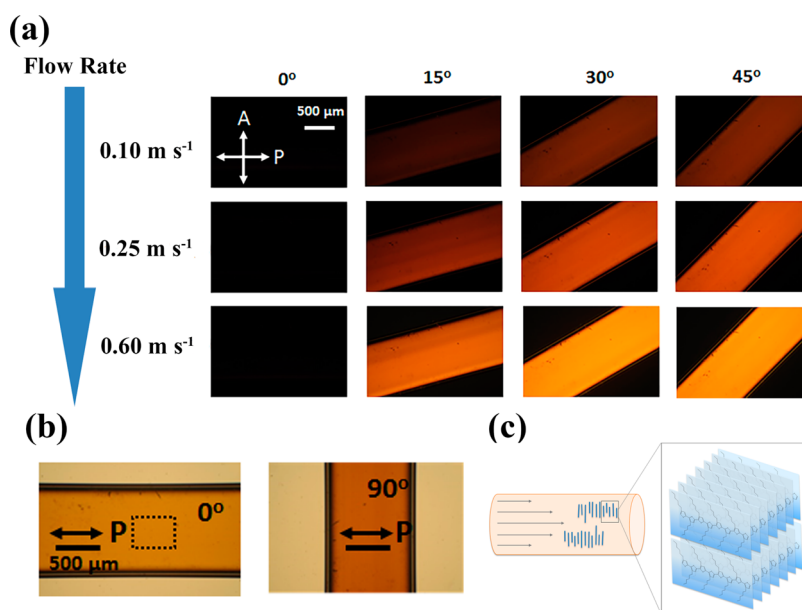
Figure 5. (a) Polarized optical microscopy (POM) images of microfluidic channels during solution flow. (b) Change in absorption as a function of capillary orientation with respect to polarizer. The image shown is a capillary at a flow rate of 0.25 m s^{-1}, displaying linear dichroism. (c) Representation of P3HT nanofibers (blue) oriented within the capillary with expected $\pi-\pi$ stacking direction along the long axis of the nanofiber. Note: Cartoon is not drawn to scale.

(no flow processing) that were loaded into glass capillaries and characterized under no flow. More details about the POM data can be found in Figures S5 and S6 in the Supporting Information.

The observed dichroism is believed to emanate from elongated $\pi-\pi$ stacked P3HT assemblies preferentially oriented parallel to the capillary long axis, as depicted in Figure 5c, with individual P3HT chains perpendicular to the capillary long axis.[43,44] The *in situ* polarized Raman spectra in Figure S7 and Table S2 further confirm the molecular orientation of assemblies in the microchannel.

Effect of Cooling and UV Radiation. Crystallization can generally be thought of as a nucleation and growth mechanism, driven by supersaturation.[45] Nucleation of polymer aggregates is thought to be induced by solution instabilities in the cooling section due to the low temperature and shear forces.[46] Fast heat and mass transfer in the microfluidic channel allow for facile control of the solution temperature, effecting the formation of highly uniform crystal nuclei, as shown in the AFM images in Figure S8 (see the Supporting Information). The mobility values in Table 1 further confirm the necessity of the flow-cooling section. After the flow-cooling section, the microchannel flows through an ambient temperature regime and is subjected to UV irradiation. Chang et al. demonstrated previously that low dose UV irradiation of P3HT solutions promotes the growth of long P3HT fibers.[47] In the sequential flow system described here, the nuclei formed in the cooling stage act as growth centers and in some sense, collect supersaturated P3HT chains. The combined effects of these two stages, coupled with shear stress,

afforded well-oriented nanofibers under laminar flow (Figure 5b, c). A control run in the absence of UV light yielded films comprised of short, disordered fibers, confirming the necessity for both the cooling and UV steps during flow processing for maximized device performance. The MCU process led to tight $\pi-\pi$ stacking with good orientation (from GIWAXS data), key points necessary to effect enhanced charge transport performance.

Effect of Flow Rate. The fluid flow rate itself had a marked effect on the resulting film morphology and device characteristics. Optimal mobility was observed at the intermediate flow rate, MCU-0.25, and can be ascribed to a combination of factors, illustrated in Figure 6. Higher shear rates cause an increase in supersaturation of the solution, as well as nucleation and growth rates, as discussed above.[48,49] The residence times in both the flow cooling and flow-UV sections were held constant across flow rates by varying the length of each microfluidic section, such that flow rate was the only relevant factor. Despite a faster growth rate at 0.60 m s^{-1}, more nuclei, which likely compete for supersaturated chains, are formed, ultimately limiting fiber length. Additionally, faster growth could cause growth with more defects. The narrower $\pi-\pi$ stacking distance found for films that underwent MCU-0.25 processing (GIWAXS data, Figure 3) suggests that these conditions represent a "sweet-spot" in the process space.

Proposed Mechanism for Solution Crystallization. The mechanism of polymer crystallization under laminar flow is the subject of intense research and is not yet fully understood.[45,50,51] However, evidence from the

literature on polymer crystallization paired with structural data analysis suggests a possible mechanism for the formation of the structural features observed in films cast from flow-processed solutions, as well as further rationale for their enhanced charge transport properties. Pennings et al. first reported the observation of bundle-like fibers formed in polyethylene solutions under flow in 1970, coining the term "shish-kebab" to describe the observed morphology.[52,53] More recently, attempts have been made to elucidate the kinetic steps of shish-kebab formation in sheared polymer solutions, indicating that the longest chains in a polymer solution undergo a coil–stretch transition

and play a catalytic role in the recruitment of other chains into elongated shish nuclei, off of which shorter chains can easily form radial lamellae.[54−56] The structure is illustrated schematically in Figure 7a. Since polymer chains' length reportedly runs along the length of the shish, $\pi-\pi$ stacking would be expected to favor the formation of kebabs. The shish-kebab structure provides a possible explanation as to why P3HT fibers demonstrate an uncommon degree of orientational alignment after flow processing, as shown in Figure 7b. Fibrillar regions in a 5 μm × 5 μm AFM image of the MCU-0.25 device were analyzed for their angle off of the horizontal using an algorithm developed by the authors [https://github.com/Imperssonator/MIC-OFET-Processing], revealing that almost all fibers are accompanied by neighboring fibers of parallel orientation. The apparent birefringence from the POM images of the films in Figure S9 may indicate enhanced conjugated polymer molecular ordering and crystallinity as well. In order for local orientational order of this degree to survive the spin-coating process, strong interfiber connections may have been formed in solution during flow processing, conceivably provided by the initial shish nucleus. Furthermore, the interfiber connections that would be afforded by a shish-kebab morphology provide additional support to the growing body of evidence that intergrain "tie chains" play a major role in determining the macroscopic hole mobility of P3HT OFETs, given the improved mobility demonstrated by flow-processed devices.[10,16,19,20,57,58] Although it is difficult to directly observe the mechanism of polymer crystallization in situ, this topic warrants further study, as it would provide insight into both the mechanism of polymer crystallization under flow
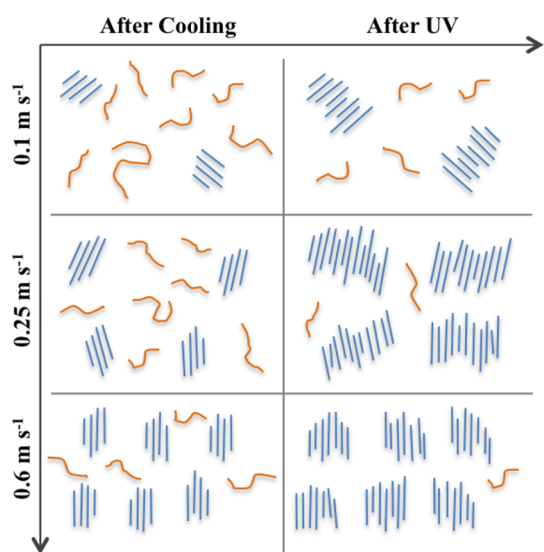

Figure 6. Proposed effect of flow rate on the nucleation and growth of P3HT nanofibers.
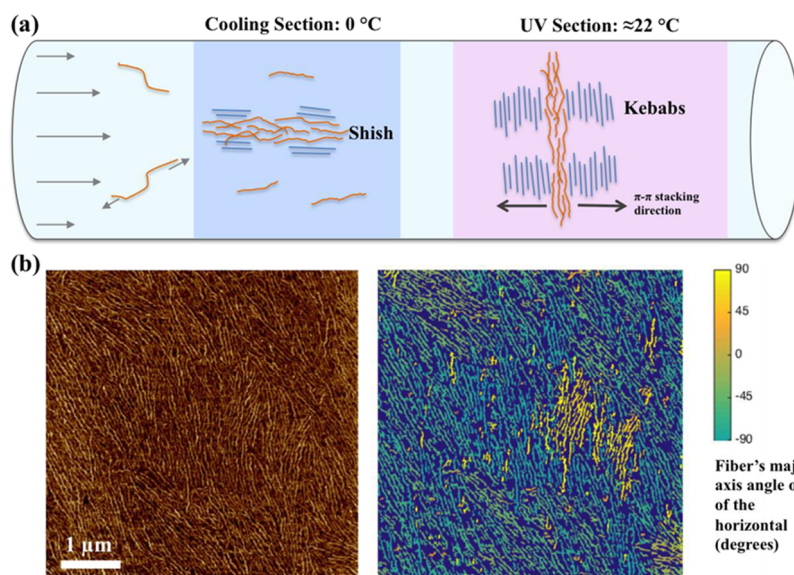

Figure 7. (a) Proposed mechanisms of nucleation and growth in the flow-cooling-UV system. In the cooling section, solution instability and shear force causes the formation of shish nuclei. The $\pi-\pi$ stacks align with the flow as they grow longer in the UV section. (b) Left: 5 μm × 5 μm AFM image of the surface of the MCU-0.25 device. Right: same image, segmented for the identification of P3HT nanofibers and their angles off of the horizontal.

and the mechanism of charge transport in conjugated polymers.

CONCLUSION

A generic solution processing strategy for high performance semiconducting polymers has been presented. Through experiments on hole (P3HT) and electron (poly(NDI2OD-T2)) transporting conjugated polymers, halogenated solvent (CHCl₃), and nonhalogenated solvent (toluene), significant mobility enhancements were attained. The facile two-step solution preprocessing method involves flow-cooling enhanced nucleation followed by flow-UV enhanced nanofiber formation. The laminar flow profile can be optimized for a given materials solution characteristics, and the process is scalable to high-throughput additive manufacturing of polymeric semiconductor devices.

Additionally, the MCU approach provided a platform to mechanistically elucidate further the nucleation and crystallization processes associated with conjugated polymer systems. Using P3HT as a model semiconducting polymer, significant dependence of film microstructure and mobility on the crystallization mechanism was identified. Evidence of an oriented crystallization mechanism provides further support for the theory that "tie chains" provide charge transport pathways between nanoaggregated structures. A general flow-processing mechanism was demonstrated which provides important insights into the process structure−property relationships operational in conjugated polymers. Guidelines for the development of high-performance devices using flow-enhanced crystal engineering were also proposed. The results position microfluidics as an accessible platform not only for the systematic study of conjugated polymer processing, but importantly the high-throughput fabrication of polymer based devices.

METHODS

Materials. P3HT was purchased from Reike Metals Inc. and used without further purification. The P3HT used in this study had a M_w of 43.9 kDa. Charge-transport poly(NDI2OD-T2) was provided by Prof. Seth Marder's group. Chloroform (anhydrous), toluene (anhydrous), and dichlorobenzene (anhydrous) were purchased from Sigma-Aldrich and used without further purification. The polytetrafluoroethylene (PTFE) pipelines with different diameters were purchased from Shanghai Liangqi Fusu Inc. The PTFE pipelines were washed with corresponding solvents three times and dried at 80 °C in a vacuum oven for 2 h before use. ¹H NMR spectra were obtained from deuterated chloroform solution at 293 K using a Bruker DSX 300. The molecular weight of P3HT was obtained through gel permeation chromatography (GPC) using trichlorobenzene as the eluent and polystyrene as the standard.

Microfluidic Shear Processing of P3HT Solutions. A microfluidic processing method was used to rapidly form a liquid crystalline solution of P3HT. The experimental setup is shown in Figure 1a.

First, a chloroform-P3HT solution was prepared: 10 mg of P3HT was introduced into 2 mL of chloroform in a 20 mL borosilicate glass vial. Alternatively, 6 mg of P3HT was introduced into 2 mL of toluene, owing to the relatively lower solubility of P3HT in toluene.

Subsequently, the vial was capped and placed on top of a hot plate for at least 30 min at ≈55 °C to ensure complete dissolution of P3HT. Then, the solution was allowed to cool to ambient temperature prior to microfluidic shear processing. A syringe pump (Remote PHD ULTRA CP syringe pump) with a glass syringe (10 mL, model 1010 LTN SYR) was used to introduce the P3HT solution into the PTFE microchannel for microfluidic processing.

As shown in the experimental setup in Figure 1a, the processing setup can be divided into two sections: (1) Flow-cooling section: The cooling bath was an ice water mixture with an average temperature of 0 °C. The cooling residence time was controlled at 1 s. (2) Flow-UV section: The PTFE microchannel was placed on the surface of a UV lamp (Entela UVGL-15, 5 mW cm⁻², 254 nm). The UV exposure residence time was held constant at 15 s.

During the microfluidic procedure, the residence time was controlled by varying the volumetric flow rate of the P3HT/CHCl3 solution via an accurate syringe pump. The microfluidic channels were flexible polytetrafluoroethylene with 300 μm inner diameter and 400 μm outer diameter. The dissolution and microfluidic shear processes were performed in air. Spin-coating of the thin films was performed about 2 min after microfluidic processing in order to limit any solution aging effects.

The Processing of Poly(NDIOD-T2) Solutions. The molecular weight of poly(NDIOD-T2) had a M_n of 128 kDa and a M_w of 217 kDa. An amount of 10 mg of poly(NDIOD-T2) was introduced into 2 mL of mixed solvents (chloroform/dichlorobenzene = 1:1 in volume) in a 20 mL borosilicate glass vial. Similar processing was carried out inside the glovebox. Only atmospheric cooling was utilized for poly(NDIOD-T2) polymer instead of the ice bath cooling used for P3HT.

Organic Field-Effect Transistor (OFET) Fabrication and Characterization. The OFET devices with bottom-gate, bottom-contact structure were fabricated to perform electrical characterization of P3HT films fabricated from solutions prepared as above. Highly n-doped silicon wafers with a thermally grown 300 nm thick SiO₂ dielectric surface were used as the substrate. The highly doped silicon substrate served as the gate electrode with the thermally grown SiO₂ as the dielectric layer. Au/Cr was used for the source and drain contacts. The source and drain contacts were fabricated using a standard photolithography based lift-off process inside a cleanroom, followed by E-beam evaporation (Denton Explorer) of 50 nm Au contacts with 3 nm of Cr as the adhesion layer.

Before spin-coating P3HT solutions, all devices were cleaned for 15 min in a UV-ozone cleaner (Novascan PSD-UV) to completely remove any residual photoresist and other organic contaminants. OFET devices were prepared by spin-coating (WS-650MZ-23NPP, Laurell) the solutions onto precleaned devices at a spin speed of 1500 rpm for 60 s in air, and tested under a nitrogen atmosphere using an Agilent 4155C semiconductor parameter analyzer. The devices were stored in a vacuum oven overnight at 50 °C and 1 Torr to remove residual solvent. The field-effect hole mobility was calculated in the saturation regime of transistor operation ($V_{DS} = -80$ V) by plotting the drain current (I_D) versus gate voltage (V_G) and fitting the data to the following equation

$$I_D = \mu C_O \frac{W}{L} (V_G - V_T) V_D \qquad (2)$$

where W (2000 μm) and L (50 μm) are the transistor channel width and length, respectively, V_T is the threshold voltage, and C_O is the capacitance per unit area of the silicon dioxide gate dielectric (1.15×10^{-8} F cm⁻²). For each condition, five OFET devices were fabricated and tested for calculation of average mobility.

Fluid Simulation of the Liquid Crystal Solution Formation. For the fluid simulation, the microchannel fabricated here was simulated using commercial software (COMSOL Multiphysics 4.4).

UV–Vis Spectroscopy. The solution and solid state UV–vis spectra were recorded using an Agilent 8510 UV–vis spectrometer. Films for solid state studies were prepared by spin-coating the requisite solution onto precleaned glass slides following the same procedures used to prepare OFET devices.

Atomic Force Microscopy (AFM). The AFM measurements were performed on films spin-coated onto bottom contact OFET devices using an ICON Dimension scanning probe microscope (Bruker) operating in tapping mode with a silicon tip (RTESP, Bruker).

In Situ Polarized Optical Microscopy (POM). The POM images were obtained with a Leica DMRX optical microscope equipped with two polarizers and a Nikon D300 digital SLR camera. The rectangular borosilicate glass capillary (0.1 mm × 1 mm × 50 mm, Vitrocom) imaged during solution flow after cooling and UV processing was fixed on a glass slide for the characterization.

In Situ Polarized Raman. Raman spectra were obtained using a $50\times$ objective and a 785 nm laser light source (Kaiser Optic System) that has 4 cm^{-1} resolution in the backscattering geometry. The laser power was 20 mW, and spectra were acquired using exposure times of 6 s with six accumulations. The sample stage was rotated from 0 to 90°, and spectra were obtained using parallel polarizers. For each spectrum, the peak corresponding to C=C stretching was fit to a Lorentzian function using Holograms software to obtain peak heights and positions.

Synchrotron Radiation Characterization. GIWAXS measurements were carried out on beamline 11−3 at the Stanford synchrotron radiation light source (SSRL). The beam was kept at an energy of 13 keV and the critical angle of measurement was 0.12°. A LaB$_6$ standard sample was used to calibrate the measurements. Using the calibration, wavelength and sample−detector distance, the 2-D images were corrected from intensity vs pixel position to intensity vs q-spacing using the software WxDiff (Figure S1). The 2-D images were subsequently reduced to 1-D plots and analyzed. Peak fitting was done using the software MagicPlot Pro.

Conflict of Interest: The authors declare no competing financial interest.

Supporting Information Available: Details on the experimental procedures, data corrections of GIWAXS, NMR, and GPC characterization, thermal stability of nanoaggregates in solutions, *in situ* POM of solutions without flow, *in situ* polarized Raman spectra of solutions confined to capillaries at the flow rate of 0.25 m s^{-1} and detailed Raman data including peak heights and area, peak fittings to obtain exciton energy from UV−visible of various films, tapping mode AFM phase images of P3HT films obtained by spin-coating from P3HT/CHCl$_3$ solutions after flow-cooling processing, and POM images of P3HT films obtained by spin-coating from P3HT/CHCl$_3$ solutions after MCU-0.25 processing. The Supporting Information is available free of charge on the ACS Publications website at DOI: 10.1021/acsnano.5b02582.

REFERENCES AND NOTES

1. Li, J.; Sun, Z.; Yan, F. Solution Processable Low-Voltage Organic Thin Film Transistors with High-K Relaxor Ferroelectric Polymer as Gate Insulator. *Adv. Mater.* **2012**, *24*, 88–93.

2. Chen, Z.; Zheng, Y.; Yan, H.; Facchetti, A. Naphthalenedicarboximide- vs Perylenedicarboximide-Based Copolymers. Synthesis and Semiconducting Properties in Bottom-Gate N-Channel Organic Transistors. *J. Am. Chem. Soc.* **2009**, *131*, 8–9.

3. Forrest, S. R. The Path to Ubiquitous and Low-Cost Organic Electronic Appliances on Plastic. *Nature* **2004**, *428*, 911–918.

4. Li, G.; Zhu, R.; Yang, Y. Polymer Solar Cells. *Nat. Photonics* **2012**, *6*, 153–161.

5. Zheng, H.; Zheng, Y.; Liu, N.; Ai, N.; Wang, Q.; Wu, S.; Zhou, J.; Hu, D.; Yu, S.; Han, S.; et al. All-Solution Processed Polymer Light-Emitting Diode Displays. *Nat. Commun.* **2013**, *4*, 1971.

6. Fu, B.; Baltazar, J.; Sankar, A. R.; Chu, P. H.; Zhang, S.; Collard, D. M.; Reichmanis, E. Enhancing Field-Effect Mobility of Conjugated Polymers through Rational Design of Branched Side Chains. *Adv. Funct. Mater.* **2014**, *24*, 3734–3744.

7. Facchetti, A. Made to Order. *Nat. Mater.* **2013**, *12*, 598–600.

8. McCulloch, I.; Heeney, M.; Bailey, C.; Genevicius, K.; Macdonald, I.; Shkunov, M.; Sparrowe, D.; Tierney, S.; Wagner, R.; Zhang, W.; et al. Liquid-Crystalline Semiconducting Polymers with High Charge-Carrier Mobility. *Nat. Mater.* **2006**, *5*, 328–333.

9. Giri, G.; Verploegen, E.; Mannsfeld, S. C. B.; Atahan-Evrenk, S.; Kim, D. H.; Lee, S. Y.; Becerril, H. A.; Aspuru-Guzik, A.; Toney, M. F.; Bao, Z. Tuning Charge Transport in Solution-Sheared Organic Semiconductors Using Lattice Strain. *Nature* **2011**, *480*, 504–508.

10. Verilhac, J.-M.; LeBlevennec, G.; Djurado, D.; Rieutord, F.; Chouiki, M.; Travers, J.-P.; Pron, A. Effect of Macromolecular Parameters and Processing Conditions on Supramolecular Organisation, Morphology and Electrical Transport Properties in Thin Layers of Regioregular poly(3-Hexylthiophene). *Synth. Met.* **2006**, *156*, 815–823.

11. O'Connor, B.; Kline, R. J.; Conrad, B. R.; Richter, L. J.; Gundlach, D.; Toney, M. F.; DeLongchamp, D. M. Anisotropic Structure and Charge Transport in Highly Strain-Aligned Regioregular poly(3-Hexylthiophene). *Adv. Funct. Mater.* **2011**, *21*, 3697–3705.

12. Chang, M.; Choi, D.; Fu, B.; Reichmanis, E.; Engineering, B.; Science, M.; States, U. Solvent Based Hydrogen Bonding: Impact on Poly (3-Hexylthiophene) Nanoscale Morphology and Charge. *ACS Nano* **2013**, *7*, 5402–5413.

13. Diao, Y.; Shaw, L.; Bao, Z.; Mannsfeld, S. C. B. Morphology Control Strategies for Solution-Processed Organic Semiconductor Thin Films. *Energy Environ. Sci.* **2014**, *7*, 2145–2159.

14. Cho, S.; Lee, K.; Yuen, J.; Wang, G.; Moses, D.; Heeger, A. J.; Surin, M.; Lazzaroni, R. Thermal Annealing-Induced Enhancement of the Field-Effect Mobility of Regioregular poly(3-Hexylthiophene) Films. *J. Appl. Phys.* **2006**, *100*, 114503.

15. Fu, Y.; Lin, C.; Tsai, F. Y. High Field-Effect Mobility from poly(3-Hexylthiophene) Thin-Film Transistors by Solvent-Vapor-Induced Reflow. *Org. Electron.* **2009**, *10*, 883–888.

16. Noriega, R.; Rivnay, J.; Vandewal, K.; Koch, F. P. V; Stingelin, N.; Smith, P.; Toney, M. F.; Salleo, A. A General Relationship between Disorder, Aggregation and Charge Transport in Conjugated Polymers. *Nat. Mater.* **2013**, *12*, 1038–1044.

17. Kim, D. H.; Park, Y. D.; Jang, Y.; Yang, H.; Kim, Y. H.; Han, J. I.; Moon, D. G.; Park, S.; Chang, T.; Chang, C.; et al. Enhancement of Field-Effect Mobility Due to Surface-Mediated Molecular Ordering in Regioregular Polythiophene Thin Film Transistors. *Adv. Funct. Mater.* **2005**, *15*, 77–82.

18. Rivnay, J.; Mannsfeld, S. C. B.; Miller, C. E.; Salleo, A.; Toney, M. F. Quantitative Determination of Organic Semiconductor Microstructure from the Molecular to Device Scale. *Chem. Rev.* **2012**, *112*, 5488–5519.

19. Kline, R. J.; McGehee, M. D.; Kadnikova, E. N.; Liu, J.; Fréchet, J. M. J.; Toney, M. F. Dependence of Regioregular poly(3-Hexylthiophene) Film Morphology and Field-Effect

Mobility on Molecular Weight. *Macromolecules* **2005**, *38*, 3312–3319.

20. Himmelberger, S.; Vandewal, K.; Fei, Z.; Heeney, M.; Salleo, A. Role of Molecular Weight Distribution on Charge Transport in Semiconducting Polymers. *Macromolecules* **2014**, *47*, 7151–7157.

21. Diao, Y.; Tee, B. C.-K.; Giri, G.; Xu, J.; Kim, D. H.; Becerril, H. A.; Stoltenberg, R. M.; Lee, T. H.; Xue, G.; Mannsfeld, S. C. B.; et al. Solution Coating of Large-Area Organic Semiconductor Thin Films with Aligned Single-Crystalline Domains. *Nat. Mater.* **2013**, *12*, 665–671.

22. Gerdts, C. J.; Tereshko, V.; Yadav, M. K.; Dementieva, I.; Collart, F.; Joachimiak, A.; Stevens, R. C.; Kuhn, P.; Kossiakoff, A.; Ismagilov, R. F. Time-Controlled Microfluidic Seeding in nL-Volume Droplets to Separate Nucleation and Growth Stages of Protein Crystallization. *Angew. Chem., Int. Ed.* **2006**, *45*, 8156–8160.

23. Diao, Y.; Helgeson, M. E.; Myerson, A. S.; Hatton, T. A.; Doyle, P. S.; Trout, B. L. Controlled Nucleation from Solution Using Polymer Microgels. *J. Am. Chem. Soc.* **2011**, *133*, 3756–3759.

24. Lim, J. A.; Liu, F.; Ferdous, S.; Muthukumar, M.; Briseno, A. L. Polymer Semiconductor Crystals. *Mater. Today* **2010**, *13*, 14–24.

25. Elvira, K. S.; Casadevall i Solvas, X.; Wootton, R. C. R.; deMello, A. J. The Past, Present and Potential for Microfluidic Reactor Technology in Chemical Synthesis. *Nat. Chem.* **2013**, *5*, 905–915.

26. Wang, G.; Shi, G.; Wang, H.; Zhang, Q.; Li, Y. In Situ Functionalization of Stable 3D Nest-like Networks in Confined Channels for Microfluidic Enrichment and Detection. *Adv. Funct. Mater.* **2014**, *24*, 1017–1026.

27. Zhao, D.; Wang, G.; He, Z.; Wang, H.; Zhang, Q.; Li, Y. Controllable Construction of Micro/nanostructured NiO Arrays in Confined Microchannels via Microfluidic Chemical Fabrication for Highly Efficient and Specific Absorption of Abundant Proteins. *J. Mater. Chem. B* **2015**, *3*, 4272–4281.

28. Wang, G.; He, Z.; Shi, G.; Wang, H.; Zhang, Q.; Li, Y. Controllable Construction of Titanium Dioxide-Zirconium Dioxide@ Zinc Hydroxyfluoride Networks in Micro-Capillaries for Bio-Analysis. *J. Colloid Interface Sci.* **2015**, *446*, 290–297.

29. Whitesides, G. M. The Origins and the Future of Microfluidics. *Nature* **2006**, *442*, 368–373.

30. Aiyar, A. R.; Hong, J. Il; Nambiar, R.; Collard, D. M.; Reichmanis, E. Tunable Crystallinity in Regioregular poly-(3-Hexylthiophene) Thin Films and Its Impact on Field Effect Mobility. *Adv. Funct. Mater.* **2011**, *21*, 2652–2659.

31. Niles, E. T.; Roehling, J. D.; Yamagata, H.; Wise, A. J.; Spano, F. C.; Moulé, A. J.; Grey, J. K. J-Aggregate Behavior in Poly-3-Hexylthiophene Nanofibers. *J. Phys. Chem. Lett.* **2012**, *3*, 259–263.

32. Aiyar, A. R.; Hong, J. Il; Izumi, J.; Choi, D.; Kleinhenz, N.; Reichmanis, E. Ultrasound-Induced Ordering in poly(3-Hexylthiophene): Role of Molecular and Process Parameters on Morphology and Charge Transport. *ACS Appl. Mater. Interfaces* **2013**, *5*, 2368–2377.

33. Zhao, K.; Khan, H. U.; Li, R.; Su, Y.; Amassian, A. Entanglement of Conjugated Polymer Chains Influences Molecular Self-Assembly and Carrier Transport. *Adv. Funct. Mater.* **2013**, *23*, 6024–6035.

34. Clark, J.; Chang, J. F.; Spano, F. C.; Friend, R. H.; Silva, C. Determining Exciton Bandwidth and Film Microstructure in Polythiophene Films Using Linear Absorption Spectroscopy. *Appl. Phys. Lett.* **2009**, *94*, 163306.

35. Delongchamp, D. M.; Kline, R. J.; Fischer, D. A.; Richter, L. J.; Toney, M. F. Molecular Characterization of Organic Electronic Films. *Adv. Mater.* **2011**, *23*, 319–337.

36. Sirringhaus, H.; Brown, P. J.; Friend, R. H.; Nielsen, M. M.; Bechgaard, K.; Langeveld-Voss, B. M. W.; Spiering, A. J. H.; Janssen, R. A. J.; Meijer, E. W.; Herwig, P.; et al. Two-Dimensional Charge Transport in Self-Organized, High-Mobility Conjugated Polymers. *Nature* **1999**, *401*, 685–688.

37. Yang, H.; Shin, T. J.; Yang, L.; Cho, K.; Ryu, C. Y.; Bao, Z. Effect of Mesoscale Crystalline Structure on the Field-Effect Mobility of Regioregular poly(3-Hexyl Thiophene) in Thin-Film Transistors. *Adv. Funct. Mater.* **2005**, *15*, 671–676.

38. Kline, R. J.; McGehee, M. D.; Kadnikova, E. N.; Liu, J.; Fréchet, J. M. J. Controlling the Field-Effect Mobility of Regioregular Polythiophene by Changing the Molecular Weight. *Adv. Mater.* **2003**, *15*, 1519–1522.

39. Salleo, A. Charge Transport in Polymeric Transistors. *Mater. Today* **2007**, *10*, 38–45.

40. Yan, H.; Chen, Z.; Zheng, Y.; Newman, C.; Quinn, J. R.; Dötz, F.; Kastler, M.; Facchetti, A. A High-Mobility Electron-Transporting Polymer for Printed Transistors. *Nature* **2009**, *457*, 679–686.

41. Xia, Y.; Callaghan, P. T. Study of Shear Thinning on High Polymer Solution Using Dynamic NMR Microscopy. *Macromolecules* **1991**, *24*, 4777–4786.

42. Born, M.; Wolf, E. *Principles of Optics: Electromagnetic Theory of Propagation, Interference and Diffraction of Light*; Cambridge University Press: Cambridge, 1999.

43. Wirix, M. J. M.; Bomans, P. H. H.; Friedrich, H.; Sommerdijk, N. A. J. M.; de With, G. Three-Dimensional Structure of P3HT Assemblies in Organic Solvents Revealed by Cryo-TEM. *Nano Lett.* **2014**, *14*, 2033–2038.

44. Kleinhenz, N.; Rosu, C.; Chatterjee, S.; Chang, M.; Nayani, K.; Xue, Z.; Kim, E.; Middlebrooks, J.; Russo, P. S.; Park, J. O.; et al. Liquid Crystalline Poly(3-Hexylthiophene) Solutions Revisited: Role of Time-Dependent Self-Assembly. *Chem. Mater.* **2015**, *27*, 2687–2694.

45. Muthukumar, M. Nucleation in Polymer Crystallization. *Adv. Chem. Phys.* **2004**, *128*, 1–63.

46. Helfand, E.; Fredrickson, G. H. Large Fluctuations in Polymer Solutions under Shear. *Phys. Rev. Lett.* **1989**, *62*, 2468–2471.

47. Chang, M.; Lee, J.; Kleinhenz, N.; Fu, B.; Reichmanis, E. Photoinduced Anisotropic Supramolecular Assembly and Enhanced Charge Transport of Poly(3-Hexylthiophene) Thin Films. *Adv. Funct. Mater.* **2014**, *24*, 4457–4465.

48. Koscher, E.; Fulchiron, R. Influence of Shear on Polypropylene Crystallization: Morphology Development and Kinetics. *Polymer* **2002**, *43*, 6931–6942.

49. Wie, J. J.; Nguyen, N. A.; Cwalina, C. D.; Liu, J.; Martin, D. C.; Mackay, M. E. Shear-Induced Solution Crystallization of poly(3-Hexylthiophene) (P3HT). *Macromolecules* **2014**, *47*, 3343–3349.

50. Cheng, S. Z. D.; Lotz, B. Enthalpic and Entropic Origins of Nucleation Barriers during Polymer Crystallization: The Hoffman-Lauritzen Theory and beyond. *Polymer* **2005**, *46*, 8662–8681.

51. Muthukumar, M.; Welch, P. Modeling Polymer Crystallization from Solutions. *Polymer* **2000**, *41*, 8833–8837.

52. Pennings, A. J.; van der Mark, J. M. A. A.; Kiel, A. M. Hydrodynamically Induced Crystallization of Polymers from Solution - III. Morphology. *Colloid Polym. Sci.* **1970**, *237*, 336–358.

53. Pennings, A. J. Bundle-like Nucleation and Longitudinal Growth of Fibrillar Polymer Crystals from Flowing Solutions. *J. Polym. Sci., Polym. Symp.* **1977**, *59*, 55–86.

54. Kimata, S.; Sakurai, T.; Nozue, Y.; Kasahara, T.; Yamaguchi, N.; Karino, T.; Shibayama, M.; Kornfield, J. A. Molecular Basis of the Shish-Kebab Morphology in Polymer Crystallization. *Science* **2007**, *316*, 1014–1017.

55. Hashimoto, T.; Murase, H.; Ohta, Y. A New Scenario of Flow-Induced Shish-Kebab Formation in Entangled Polymer Solutions. *Macromolecules* **2010**, *43*, 6542–6548.

56. Mykhaylyk, O. O.; Chambon, P.; Impradice, C.; Fairclough, J. P. A.; Terrill, N. J.; Ryan, A. J. Control of Structural Morphology in Shear-Induced Crystallization of Polymers. *Macromolecules* **2010**, *43*, 2389–2405.

57. Lan, Y.-K.; Huang, C.-I. A Theoretical Study of the Charge Transfer Behavior of the Highly Regioregular Poly-3-Hexylthiophene in the Ordered State. *J. Phys. Chem. B* **2008**, *112*, 14857–14862.

58. Lan, Y.-K.; Huang, C.-I. Charge Mobility and Transport Behavior in the Ordered and Disordered States of the Regioregular poly(3-Hexylthiophene). *J. Phys. Chem. B* **2009**, *113*, 14555–14564.